

Chapter 6

Characterization of Lead Halide Perovskites Using Synchrotron X-ray Techniques



Lijia Liu and Zhaohui Dong

Abstract In this chapter, we are going to introduce several characterization methods that utilize synchrotron X-rays as the probing source for understanding electronic structure, crystal structure, and optical properties of lead halide perovskite materials. We will show how X-ray absorption fine structure (XAFS) can be used to understand the dissociation mechanism, to identify the presence of defect, and to analyze the influence of dopant introduction on structural modification. We will demonstrate that an X-ray excited optical luminescence (XEOL) in combination with XAFS analysis helps to understand the luminescence mechanism of doped perovskite. We will also present the use of synchrotron X-ray diffraction (XRD) to study the creation of new crystal phases induced by high pressure and the phase transformation of perovskite in situ. The working principle of each technique will be introduced, followed by examples from recently published research articles.

6.1 Introduction

Lead halide perovskites (LHPs) has attracted great attention since its first successful application in solid-state dye-sensitized solar cells in 2012 [1]. Potential applications of LHPs have been extended to many fields, such as solar cells, light-emitting devices, catalysis, and lasers [2, 3]. LHP has a perovskite-type structure of ABX_3 , in which A is a small organic alkylamine cation (typically $CH_3NH_3^+$ or $NH_2CH = NH_2^+$) or a heavy alkaline cation (i.e. Cs^+), B is Pb^{2+} , and X is a halide (Cl^- , Br^- , or I^-). The band gap of LHPs can be easily tuned throughout the entire visible wavelength by adjusting the composition of halide ion species and/or the nanocrystal size through

L. Liu (✉)

Department of Chemistry, University of Western Ontario, 1151 Richmond Street, London, ON N6A 5B7, Canada
e-mail: lijia.liu@uwo.ca

Z. Dong

Shanghai Synchrotron Radiation Facility (SSRF), Shanghai Advanced Research Institute, Chinese Academy of Science, Shanghai 201204, People's Republic of China
e-mail: dongzhaohui@zjlab.org.cn

quantum size-effect [4]. The I-based LHPs (ABi_3) absorbs red light, making them suitable for solar cell applications. The power conversion efficiency of LHP solar cell has significantly improved since it was first used in dye-sensitized solar cells in 2009 [5]. As the light absorbing material in solar cell, LHPs have demonstrated suitable band gap and trap-state density, high absorption coefficient, and long carrier diffusion lengths [6, 7]. Br- and Cl- based LHPs, on the other hand, have slightly larger band gap, and are more widely used for light-emitting applications. As a light-emitter, they exhibit single-color emission, high photoluminescence quantum yield (PLQY) [3]. By introducing additional divalent or trivalent ions as dopants, the PLQY of intrinsic LHP can be further enhanced [8, 9], and some dopant ions introduce additional radiative recombination paths, making LHP a dual-color light emitter [10, 11].

Although LHPs have brought exciting opportunities for the optoelectronics market, commercial applications are still challenging. Stability and toxicity are two major concerns LHP-based devices. The organometal LHPs are unstable under light, heat, and oxygen [12, 13], and almost all LHPs are vulnerable to moisture [14]. For example, bare methylammonium lead iodide (MAPbI_3) thin films are only stable in an oxygen- and water-free environment. Bare CsPbBr_3 suffers serious photoluminescence loss under sustained operational conditions [15, 16]. The presence of Pb in LHP also raises environmental safety concern if LHP-based devices are produced in large quantity. Although attempt has been made to synthesis Pb-free perovskites for optoelectronic applications, the device performance is not satisfactory [17, 18]. To address these issues, a deep understanding on the fundamental properties of LHPs is essential. In this chapter, we will provide a summary on a series of characterization techniques for LHP research that utilize X-rays generated from synchrotron radiation.

Synchrotron radiation is produced by accelerating electrons approaching the speed of light. When the electrons are directed in a curved orbit under magnetic field, electromagnetic radiation is produced tangentially to the orbit. The energy of the electromagnetic radiation covers a wide range, from near-infrared to hard X-ray, and a monochromator is used for energy selection to meet specific research needs. For research that involves the use of X-rays, synchrotron X-ray has several advantages over the traditional X-ray sources: (1) the photon energy is tunable from soft X-ray (a few tens of eV) to hard X-rays (several tens of keV); (2) the photon flux is more than 10 orders of magnitude than traditional X-rays; (3) it can provide highly collimated beam with spatial resolution down to several microns or in some cases, several tens of nanometers; (4) the photons can be either linearly or circularly polarized which allows polarization-dependent studies; (5) electrons can be produced in bunches with the use of radio frequency cavities inserted in their travelling orbit. The emitted light in this case is pulsed with a few nanoseconds between pulses, which allows time-resolved spectroscopy.

Several synchrotron X-ray spectroscopic and microscopic techniques have been successfully applied on studying the fundamental properties of LHP materials and LHP-based optoelectronic devices. For example, X-ray absorption fine structure

(XAFS) is used to study the degradation mechanism and local structural defect [19–21]; X-ray excited optical luminescence (XEOL) spectroscopy provides evidence on the luminescence mechanism of ion-doped LHP [22]; X-ray diffraction (XRD) acquired under high pressure can track the crystal structure evolution during phase transformation and allows identification of new crystal phases [23, 24]; X-ray photoelectron spectroscopy (XPS) studies the surface composition and perovskite-ligand charge transfer [25, 26]; X-ray scattering helps to understand formation and orientation of crystalline grains in perovskite films [27, 28]. In the following, we will focus on three X-ray probing techniques, which are XAFS, XEOL and XRD, and demonstrate how synchrotron X-ray helps in materials analysis with particular emphasis on LHP materials. The goal of this chapter is to provide insight on using these spectroscopic techniques to guide future material synthesis and device design.

6.2 Techniques and Applications

6.2.1 X-ray Absorption Spectroscopy

X-ray absorption spectroscopy (XAS) measures the absorption behavior of materials as a function of incident photon energy. XAS can only be performed using a synchrotron source, where tunable X-ray source is provided. There are several excellent resources that provide detailed theory background as well as data analysis protocols [29, 30]. The readers are welcome to refer to them for an in-depth learning on such technique. In the following, we outline the basic working principle of XAS and the key knowledge required to understand the results discussed in literatures.

6.2.1.1 Working Principle

XAS measures the absorption coefficient of a material upon interacting with incident X-rays. The general absorption principle follows the Beer's law as:

$$I_t = I_0 e^{-\mu l} \quad (6.1)$$

in which I_0 is the intensity of incident photons, I_t is the intensity of the transmitted photons, l is sample thickness and μ is the absorption coefficient. The absorption coefficient μ depends on (1) the type of atoms in the materials, (2) how they are distributed and their bonding environment, and (3) the polarization and energy of the X-rays. Experimentally it is determined by comparing the intensities of incident light and the ones passing the material with known thickness.

For a monatomic sample, once the incident energy (E_{ex}) is sufficient to promote an electron from a core level to a previously occupied energy level, there will be an abrupt increase in the absorption coefficient. The absorption spectrum (Fig. 6.1a)

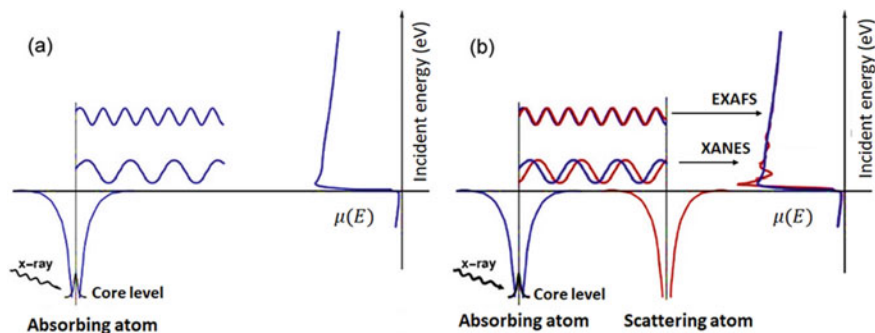


Fig. 6.1 Schematic illustration of the outgoing photoelectron wave produced by **a** a free atom and **b** a diatomic system upon X-ray absorption and the corresponding XAFS spectrum

exhibits a flat line at energy lower than the absorption threshold, followed by a sharp rise in intensity, then a monotonic decay. The energy (E_0) where the intensity rise occurs is referred to as an absorption edge (or simply, an edge). Above E_0 , photoelectrons are created which travel as a wave with wavenumber proportional to $\sqrt{E_{ex} - E_0}$. Table 6.1 lists the letter symbols that label the absorption edges and the corresponding electronic transitions. The edge energy E_0 is dependent on the type of element and the energy level of the electron being excited. The detailed values are available in the X-ray data booklet [31]. Please note that these tabulated values apply to monatomic elements. For compounds that contain multiple atoms, some deviation occurs, which is used to identify the change in oxidation states of the element and their surrounding chemical environment.

If the excited electrons are from an element in a polyatomic compound, the outgoing photoelectron wave will be interfered with the neighboring atoms. The construction and destruction waves between outgoing and backscattered photons modulate absorption coefficient $\mu(E)$ and create oscillations in absorption intensities above E_0 , producing X-ray absorption fine structure (XAFS), shown in Fig. 6.1b.

Table 6.1 Symbols for absorption edges and the corresponding electronic transition

Principal quantum number	Absorption edge	Electronic transition
1	K	$1s \rightarrow np$
2	L₁	$2s \rightarrow np$
	L_{2,3}	$2p_{1/2,3/2} \rightarrow ns, nd$
3	M₁	$3s \rightarrow np$
	M_{2,3}	$3p_{1/2,3/2} \rightarrow ns, nd$
	M_{4,5}	$3d_{3/2,5/2} \rightarrow np, nf$

Content in bold is the ones that are most frequently measured

In terms of data interpretation, XAFS is usually divided into two energy regions. From a few eV below E_0 to 50 eV above is the region of X-ray absorption near-edge structure (XANES). In XANES, the modulation of $\mu(E)$ is mainly caused by multiple scattering from surrounding atoms, because the kinetic energy of outgoing photoelectrons is low. It is highly sensitive to the local chemical environment, such as oxidation states, unoccupied electronic states, and local symmetry, so it can be used as “fingerprints” of the materials. At this region, the outgoing signal is dominated by single scattering, and the modulation of the absorption coefficient is be.

From 50 eV up to 1000 eV above the edge, the strong oscillations start to disappear. This is the region of extended X-ray absorption fine structure (EXAFS). EXAFS is dominated by single scattering (the outgoing electron has a high kinetic energy). Local structures such as bond length within first 2 or 3 atomic shells can be obtained by analyzing the EXAFS data [32, 33]. The application of EXAFS is not limited to solid powders, thin films, liquids, and devices in operando can also be directly measured at the experimental stations [34].

Data analysis of EXAFS is less intuitive. As seen in Fig. 6.1b, at the EXAFS region, the intensity oscillation is much weaker compared to the one at the XANES region, therefore a “fine-structure” function $\chi(E)$ is introduced to define the change in absorption amplitude as a function of X-ray energy:

$$\chi(E) = \frac{\mu(E) - \mu_0(E)}{\Delta\mu_0(E)} \quad (2.2)$$

where $\mu(E)$ is the measured absorption coefficient, $\mu_0(E)$ represent the absorption of an isolated atom (i.e. the background), and $\Delta\mu_0(E)$ is the amount of jump in intensity at the absorption threshold. Since the spectral oscillation diminishes quickly above the absorption edge, the spectrum is also converted from the X-ray energy space (E-space) to the wavenumber space (k-space). The conversion is shown in the equation:

$$k = \sqrt{\frac{2m(E - E_0)}{\hbar^2}} \quad (2.3)$$

The function, $\chi(k)$, is referred to as the “EXAFS”. It is a summary of scattering waves, which is from the interference with different atoms sitting in the near-neighbor coordination shells. A Fourier transform of the EXAFS spectrum provides photoelectron scattering profile as a function of the radial distance from the absorbing atom. EXAFS displayed in this way is referred to as the “R-space” profile.

The full EXAFS equation has the expression:

$$\chi(k) = \sum_j \frac{N_j S_0^2 f_j(k) e^{-2k^2 \sigma_j^2} e^{-2R_j/\lambda_j(k)}}{k R_j^2} \sin[2kR_j + \delta_j(k) + 2\varphi_C(k)] \quad (2.4)$$

where N_j is the number of the neighboring atoms in the j th coordination shell, S_0^2 is the amplitude reduction factor, $f(k)$ and $\delta(k)$ are scattering properties of the neighboring atoms, $\varphi_C(k)$ is the phase-shift of the absorbing atom, R is the distance to the neighboring atom, and σ^2 is the disorder in the interatomic distance. Quantitative analysis of EXAFS helps to determine the local structure of the absorbing atoms, including parameters such as coordination numbers, interatomic distances, and degree of structural disorder. This is performed by first establishing a structure model, and use this model to generate the scattering parameters in the EXAFS equation to fit the measured EXAFS spectrum. These calculated parameters will then be used to predict and modify the guessed structural parameters until a best fit is obtained.

The choice of XAFS techniques depends on specific scientific questions to be addressed. In the next two sections, we are going to demonstrate how XANES and EXAFS are used in advancing the knowledge on perovskite materials.

6.2.1.2 XANES using Soft X-rays: The Dissociation Mechanism

Soft X-rays usually refer to X-rays with energy lower than 2000 eV, which is suitable for studying low Z elements (first two rows of the main group elements in the periodical table and some transition metals). At this range, the energy separation between adjacent absorption edges are small, so EXAFS is often not feasible. Instead, XANES is the main focus, and the rich spectral features at this region is useful for identifying chemical species and the oxidation state of the element of interests. For characterization of perovskites, XANES has been used to study the alignment of the cation groups [35, 36] and the band structure of formamidinium lead halide [37]. In the following, we will focus on the research dissociation mechanism study of methylammonium lead halide (MAPbI₃).

The first generation of LHP for optoelectronic application has a hybrid structure, which contains inorganic framework PbI₆²⁻ and organic methylammonium cations CH₃NH₃⁺ [38]. This hybrid perovskite has a chemical formula of CH₃NH₃PbI₃ (MAPbI₃), and can be easily synthesized by mixing two precursors CH₃NH₂ and PbI₂ in an organic solvent such as γ -butyrolactone [5]. MAPbI₃ has a black color, which is ideal for light harvesting. As the light absorbing layer in photovoltaic cells, MAPbI₃ (or MAPbI_{3-x}Cl_x) has long carrier diffusion lengths and low charge recombination rates [6, 39]. However, the greatest challenge for commercialization of MAPbI₃-based solar cell is the insufficient lifetime. MAPbI₃ is vulnerable to various environmental factors, such as water, temperature, and UV-exposure [12–14]. There are several decomposition mechanisms proposed by several groups and there is still controversy among them [40, 41]. Aside from decomposition, there is also possible by-product that co-exist with MAPbI₃, and might play a negative role in the photovoltaic performance. It is therefore crucial to identify the chemical species present in thin film MAPbI₃.

The corner-sharing octahedral PbI₆²⁻ framework is relatively stable. The CH₃NH₃⁺ cations sitting between those octahedra are vulnerable to decomposition.

The presence of multiple carbon species in MAPbX₃ films have been observed using X-ray photoelectron spectroscopy by various researchers [42–44]. It is however, difficult to identify the origin of the carbon species. Some might be related to carbon impurities in the environment, but for MAPbI₃ prepared under vacuum, dual carbon species were also observed [45].

XANES at the C K-edge has been successfully used as a probe for the carbon species in MAPbI₃ [19]. Two MAPbI₃ films were investigated: one is freshly prepared MAPbI₃ film, and the other is a film prepared with identical method but under prolonged X-ray exposure prior to XANES measurement. Figure 6.2, XANES of both films contain a sharp peak at ~282 eV, followed by a doublet at higher energy side. The ratio between the low energy and high energy feature differs between the two samples. To better interpret the spectra, simulated XANES based on a perfect cubic MAPbI₃ was included for comparison. From the simulated result, we can see only features at high energy were reproduced. The low energy peak does not belong to a perfect MAPbI₃ structure. Instead, if the C–N bond length in the CH₃NH₃⁺ unit is stretched, a new peak appears at the low energy, and the separation between the

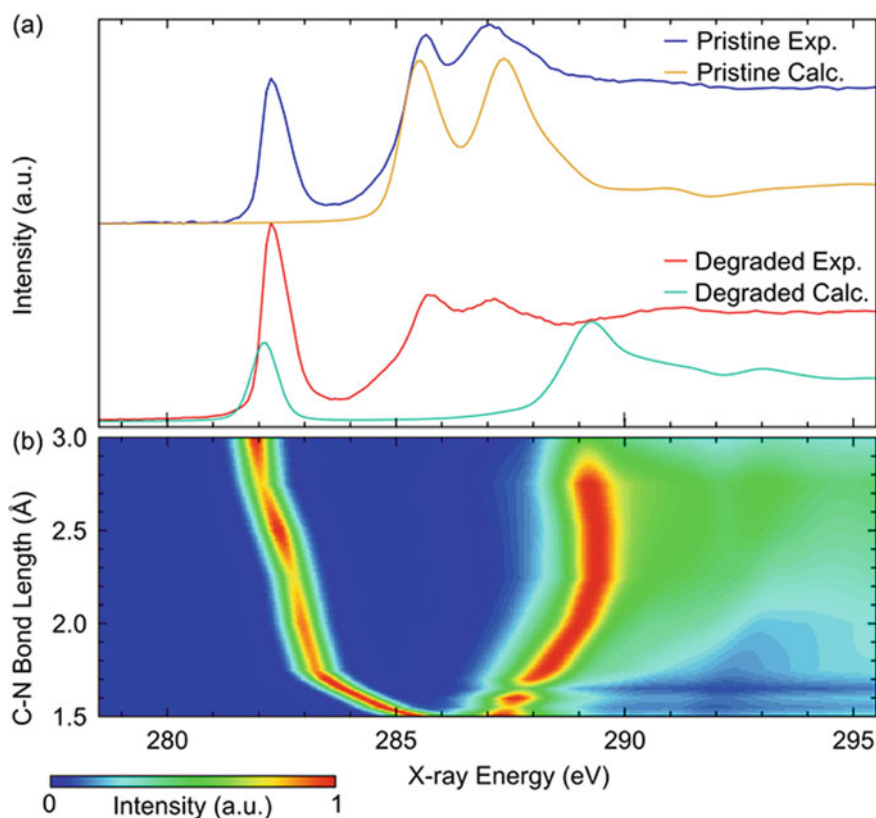


Fig. 6.2 XANES at the C K-edge of a MAPbI₃ thin film. Adapted from Ref. [19]

new peak and the main peak increases as the C–N bond length increases. Therefore, a possible dissociation mechanism of MAPbI₃ was proposed: CH₃NH₃⁺ decomposes into CH₃⁺ which further bonds to iodide of the main PbI₆²⁻ framework, and NH₃ migrates out of the perovskite lattice as a neutral molecule. This hypothesis was also supported by other characterization results such as X-ray photoelectron spectroscopy and mass spectroscopy [45–48].

It is worth mentioning that another study also used the C K-edge XANES to identify the organic species in MAPbI₃ thin films, shown in Fig. 6.3 [20]. In this study, the XANES spectra were analyzed by peak fitting, which is done by first defining a step function as the background (single-atom absorption), and fit the main resonance with several Gaussian peaks. The PEY and TEY in the figure refer to partial electron yield and total electron yield, respectively. In this analysis, a neutral CH₃NH₂ species was identified. Comparing with the C K-edge XANES of MAPbI₃ in Fig. 6.2, the apparent difference is that the low energy feature is absent in this study. One possible explanation is that the spectra acquired in the two studies probe samples at different depths. XANES in Fig. 6.3 were recorded with electron yield, which has a shallow probing depth (25 nm for TEY and 6 nm for PEY), while the ones in Fig. 6.2 were recorded in fluorescence yield, which has probing depth greater than 200 nm. The dissociation occurs in the bulk rather than on the surface. The calculation also suggests that neutral CH₃NH₂ cannot reside stably inside the MAPbI₃ lattice, but rather resides mainly on the surface or at grain boundaries of thin films [20].

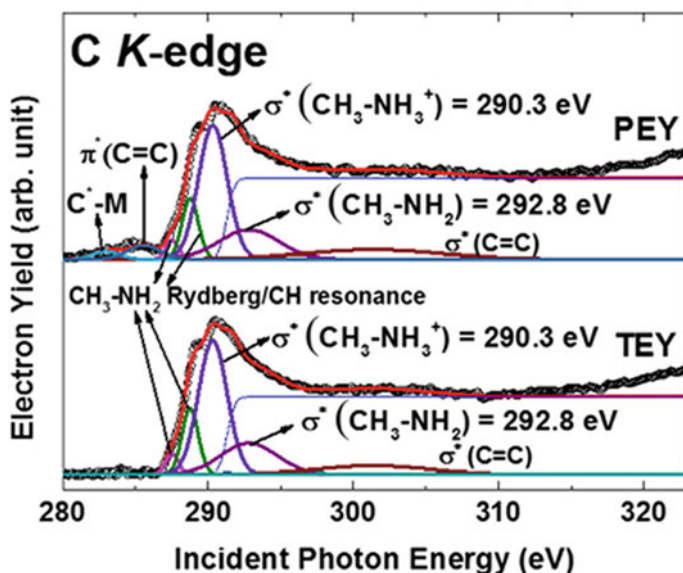


Fig. 6.3 The C K-edge XANES of MAPbI₃ film acquired with PEY and TEY. Curve fitting and the assignment of the composition were indicated in the figure. Adapted from Ref. [20]

6.2.1.3 EXAFS using Hard X-rays: The Local Structure Probe

As a structure probe, EXAFS has been used to analyze perovskite thin films and nanocrystals. The coordination environment of Pb extracted from the Pb L_3 -edge EXAFS can be correlated with the stability of LHP and the performance of LHP-based optoelectronic devices. There are reports on using the Pb L_3 -edge EXAFS to study the temperature and light-induced degradation product of MAPbI_3 , and the non-LHP species such as metallic Pb and PbI_2 can be identified by their characteristic bonding environment [49, 50].

Although an ideal perovskite structure contains PbX_6^{2-} octahedral units in which Pb is 6-coordinated with halide ions, in practical case, as-synthesized MAPbI_3 contains various intrinsic defects [51, 52]. The presence of halide vacancies are beneficial for charge transport, but too much vacancies will act as traps which cause negative impact on the device performance [53]. It was found that adding a small amount of Cl in MAPbI_3 drastically improves the power conversion efficiency of MAPbI_3 -based solar cells [54]. However, the ratio of Cl and I need to be precisely tuned to achieve the best performance. The “magic ratio” of the two halide precursors, $\text{CH}_3\text{NH}_3\text{I}$ and PbCl_2 is optimized to be 3:1 and confirmed by multiple studies. An EXAFS study was conducted to examine how the perovskite structure is affected by the precursor concentrations [21]. Figure 6.4, EXAFS was displayed at R-space and k-space, respectively, and a multiple-shell fitting model was used including Pb-Cl, Pb-I, and Pb-C/N scattering paths. The results show that the halide vacancies vary when different ratios of PbCl_2 and $\text{CH}_3\text{NH}_3\text{I}$ were used. The power conversion

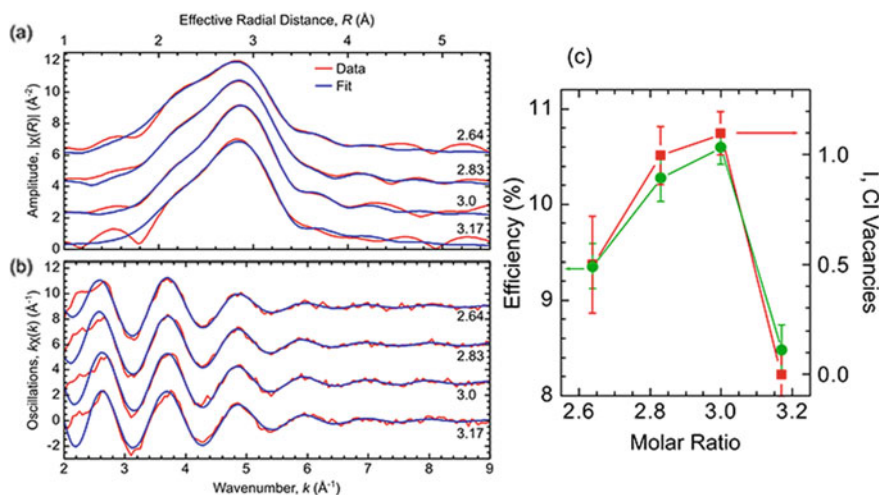


Fig. 6.4 The Pb L_3 -edge EXAFS of $\text{MAPbI}_{3-x}\text{Cl}_x$ prepared with different I: Cl ratios. The spectra are shown in **a** k-space and **b** R-space, respectively, with both experimental and fitted results. **c** The power conversion efficiencies and the halide vacancies plotted as a function of precursor ratio. Adapted from Ref. [21]

efficiencies of solar cells align perfectly with the amount of vacancies. MAPbI₃ with highest halide vacancies is achieved at the optimal 3:1 precursor ratio. Higher or lower ratio produces fewer vacancies and hinders the solar cell performance.

Doping ions into perovskite has demonstrated great potential in modifying the light-emitting properties of perovskites. For example, Mn²⁺-doped CsPbCl₃ exhibits orange emission [10, 55]. Yb³⁺-doping of CsPbCl₃ makes it a near-infrared light emitter [56]. CsPbCl₃ nanocrystals co-doped with Bi³⁺ and Mn²⁺ emit white light [57]. The intrinsic luminescence of CsPbX₃ can be greatly enhanced by introducing Ni²⁺, Cu²⁺, and Y³⁺ [8, 58, 59]. We will show in Sect. 2.2 how synchrotron X-rays is used to study the luminescence mechanism of doped perovskite. In this section, we focus on the use of EXAFS technique in studying the local structure of dopant ions as well as how the main LHP framework is influenced upon dopant introduction.

EXAFS provides direct evidence that dopant introduction greatly impacts the pristine structure of the Pb-X framework. It was reported that Ni²⁺ doping greatly enhances the intrinsic luminescence of CsPbX₃ regardless of the halide species. EXAFS at the Pb L₃-edge reveals that the luminescence enhancement is due to an improved short-range order of the CsPbX₃ lattice [58]. Similar phenomenon was also observed in Cu-doped CsPbBr₃. Doping significantly enhances the thermal stability and photoluminescence quantum yield of CsPbBr₃. Figure 6.5 shows the Pb L₃-edge EXAFS in k-space and R-space of Cu-doped CsPbBr₃ [8]. The detailed structural parameters derived from the fitting are summarized in Table 6.1. It was found that upon doping, the Pb-Br bond length decreases slightly due to lattice contraction. Such contraction increases the interaction between Pb and Br, and improves the formation energy of the CsPbBr₃ lattice. The coordination number of Pb is greatly increased, suggesting that doping reduces halide vacancies, and therefore enhance the luminescence intensity of CsPbBr₃.

EXAFS of the dopant ions can also be measured. In most of the cases, the R-space spectra at the dopant absorption edge show reduced dopant-halide bond length. This has been attributed to the smaller ionic radius of the substitute ions

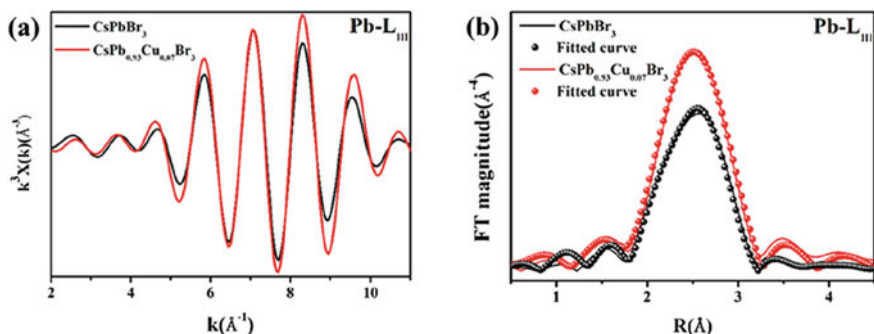


Fig. 6.5 EXAFS spectra of CuPbBr₃ and Cu-doped CsPbBr₃ quantum dots. **a** k_3 -weighted EXAFS in k-space, **b** Fourier transformed R-space EXAFS. Adapted from Ref. [8]

[8, 58, 60]. However, due to the low doping concentration, quantitative EXAFS analysis is limited, presumably due to the low signal to noise ratio at energy well-beyond the absorption edge.

6.2.2 X-ray Excited Optical Luminescence (XEOL)

6.2.2.1 The Working Principle

Upon photon absorption, electrons are promoted to the previously unoccupied electronic states, and settled at the bottom of the conduction band, while holes drift to the top of the valence band. Radiative recombination of electron-hole pairs produces luminescence. Luminescence can be produced with visible and UV light excitation, such as the light source used in conventional laboratory spectrofluorometer. X-ray on the other hand, can also be used as an excitation source, and the production of luminescence is illustrated in Fig. 6.6. During this process, core-electrons are excited, and the holes leaving behind undergoes a series of thermalization processes to reach the top of the valence band of the materials. During thermalization, electrons at shallower levels fill the core hole, producing Auger electrons and a hole at an outer shell. The energetic electrons continue to travel in the solid, losing its energy and producing shallower core holes. This cascade process is repeated until holes are created at the top of the valence band, and recombine with electrons at the bottom of the conduction band.

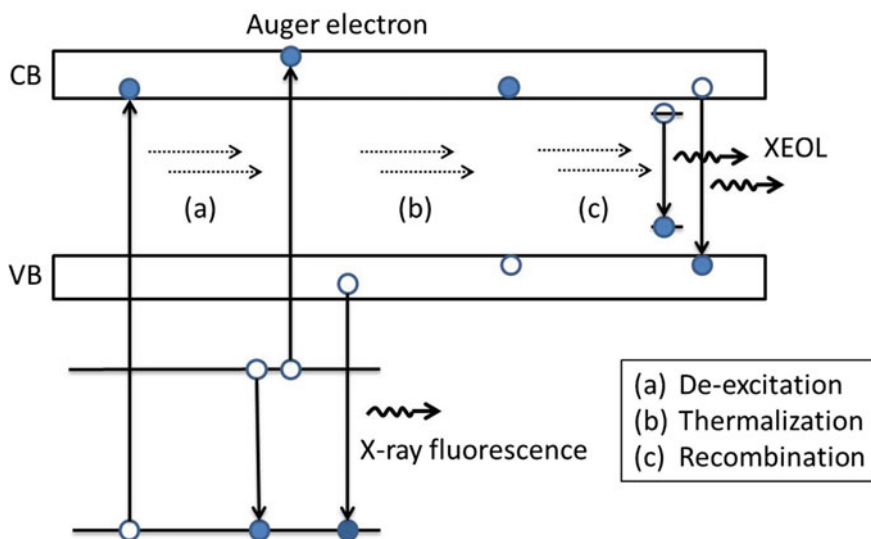


Fig. 6.6 Schematic illustration of the production of luminescence following a core-electron excitation with X-ray

The biggest advantage of using X-ray as the excitation source is that the wavelength and intensity of the emitted light can be related to the de-excitation process of electrons at a particular core-level. X-ray excited optical luminescence (XEOL) is often collected at the same energy range as one chooses to acquire an XAFS spectrum of an element of interest. The light emission can then be related to the absorption behavior of the material. By tracking the XEOL profile as a function of excitation energy, the origin of the luminescence can be identified [61]. A combined XEOL-XANES analysis has been successfully used in understanding luminescence mechanism of heterostructures, nanostructured metal oxides, solid solutions and organic light-emitting materials [61–63].

For bright light-emitting materials, XEOL is collected simultaneously with XANES, generating a 2D contour plot, shown in Fig. 6.7a. The horizontal axis is the excitation energy, the vertical axis is the wavelength, and the color-coded z-axis is the intensity of the emitted light. In this plot, the excitation energy-dependency of luminescence can be visualized: the horizontal cut of the contour map shows an XEOL spectrum at a selected excitation energy, and the intensity variation of emission at certain wavelength can be obtained from a vertical cut from the map. For weak light-emitting materials, XEOL can be collected at selected excitation energies, where abrupt change in absorption coefficient occurs, shown in Fig. 6.7b. The intensity and emission profile change as a function of excitation energy can be interpolated.

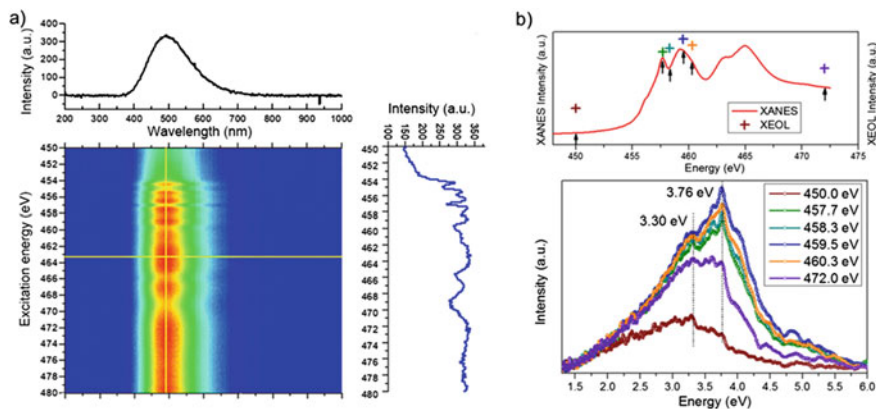


Fig. 6.7 a) a 2D XANES-XEOL contour plot of TiO_2 nanowires. A horizontal cut (XEOL spectrum) and a vertical cut (intensity variation at maximum XEOL as a function of energy) are shown on top and on the right of the contour plot, respectively. Adapted from Ref. [64] b) top: integrated XEOL intensities (cross marks) of TiO_2 nanograss at selected excitation energies (indicated by arrows) in comparison with the $\text{Ti L}_{3,2}$ -edge XANES. Bottom: XEOL spectra of nanograss under selected excitation energies. Adapted from Ref. [65]

6.2.2.2 XEOL-XAFS Analysis: Luminescence Mechanism

Ion doping of CsPbCl₃ and CsPbBr₃ has been demonstrated an effective strategy of modifying their luminescence properties. In particular, Mn²⁺ doping introduces an additional emission band at the orange–yellow region. Detailed charge transfer mechanism was investigated by an XEOL-XANES analysis on Mn²⁺-doped CsPb(Cl/Br)₃ nanocrystals [22]. The nanocrystals exhibit dual emission bands, similar to most of the Mn-doped LHPs. The blue emission at ~430 nm is from the near band-gap recombination of perovskite host lattice, and the orange emission at ~600 nm is from the Mn d–d transition between the ⁴T₁ and ⁶A₁ configurations [10, 66].

Shown in Fig. 6.8, the XANES at the Mn L_{3,2}-edge of Mn-doped CsPb(Br/Cl)₃ has typical Mn²⁺ features. Several XEOL spectra were recorded at selected excitation energies from below to above the Mn absorption edge. It is interesting to observe that not only the intensity of the luminescence is dependent on the excitation energy, a minor wavelength shift of the perovskite near-band-gap emission is also observed. Careful analysis reveals that this near-band-gap emission in fact contains two components: one is excitation energy-dependent, while the other is less sensitive to the excitation energy. When the Mn electrons absorb most of the incoming photons, a decrease in the Mn-related emission was observed. This suggests that

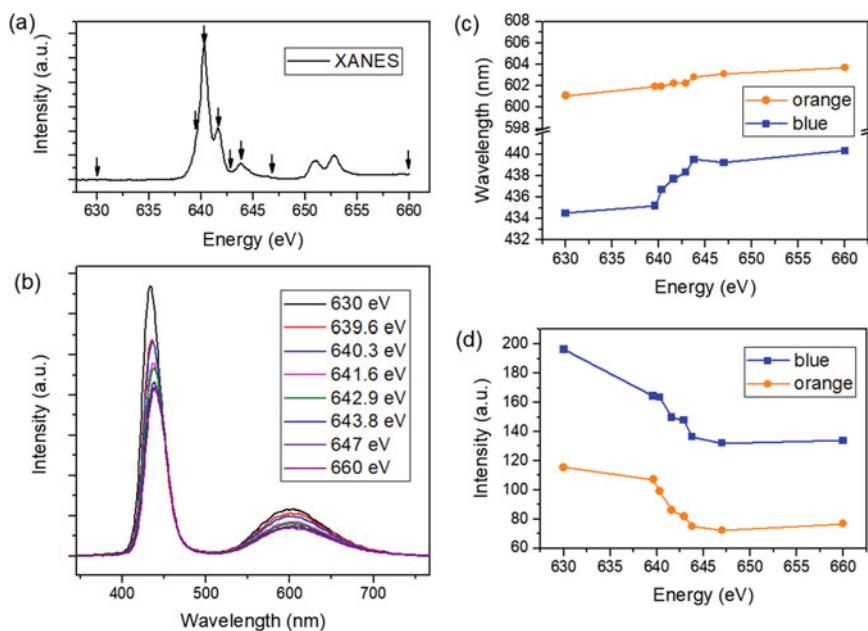


Fig. 6.8 Excitation energy-dependent luminescence of Mn-doped CsPb(Br/Cl)₃. **a** Energy selection from the XANES spectrum. **b** XEOL at each excitation energy. **c** The trend of emission peak wavelength as a function of excitation energy for each emission band. **d** The trend of emission peak intensity as a function of excitation energy for each emission band. Adapted from Ref. [22]

directly promoting the electronic transition in Mn is not the effective radiative recombination channel. Instead, luminescence from Mn-doped CsPb(Br/Cl)₃ is facilitated by energy transfer from the excitons formed within the perovskite host lattice.

6.2.3 X-ray Diffraction (XRD)

6.2.3.1 XRD with Synchrotron Radiation

X-ray diffraction (XRD) is the most commonly used technique for determination of crystal structure at atomic resolution. The basic principle for XRD is given by the Bragg equation:

$$\lambda = 2d_{hkl} \sin \theta \quad (6.5)$$

where λ is the wavelength of the incident X-ray, d_{hkl} is the spacing of the lattice planes with the Miller indices h , k , l , and θ is the angle of specular reflection with respect to these planes. The diffraction angle, defined as the angle between the incident primary beam and the diffracted beam, is therefore equal to 2θ .

Laboratory XRD and synchrotron XRD share the same diffraction principle, although X-rays are produced from different sources. Laboratory XRD uses X-rays generated from electrons hitting a metal anode, such as Co, Cu, and Mo. For a specific type of metal, the energy of the X-ray is a fixed value. Synchrotron X-rays, on the other hand, provides a wide selection of energy range. In addition, synchrotron X-rays are several orders more intense, which makes it possible to obtain high quality diffraction data with higher resolution, lower background to peak intensity ratios, and shorter collection time. Therefore, XRD collected with synchrotron are more favorable for structure resolving. High energy X-rays has stronger penetrating ability than lab X-rays, making it suitable to adapt sample of various physical forms. In particular, in situ XRD can be easily achieved at synchrotron X-ray station. In addition, collimated X-rays from synchrotron can achieve micron to a few hundred of nanometer spatial resolution, which allows mapping the crystal structure distribution on a surface.

Various types of synchrotron-based XRD techniques have been developed, such as angle dispersive XRD (ADXRD) and energy dispersive XRD (EDXRD), shown in Fig. 6.9a,b, respectively. In both techniques, data acquisition is conducted in a transmission mode, which means the incident X-ray and the detector are located at different side of the sample. This requires either the energy of the X-ray is high enough or the sample is sufficiently thin for X-ray to penetrate. ADXRD uses a monochromatic beam as the source, and the diffraction pattern is collected from all solid angles. EDXRD, on the other hand, is almost exclusively performed using synchrotron X-rays. It uses polychromatic photons as the incident source and the detector is place

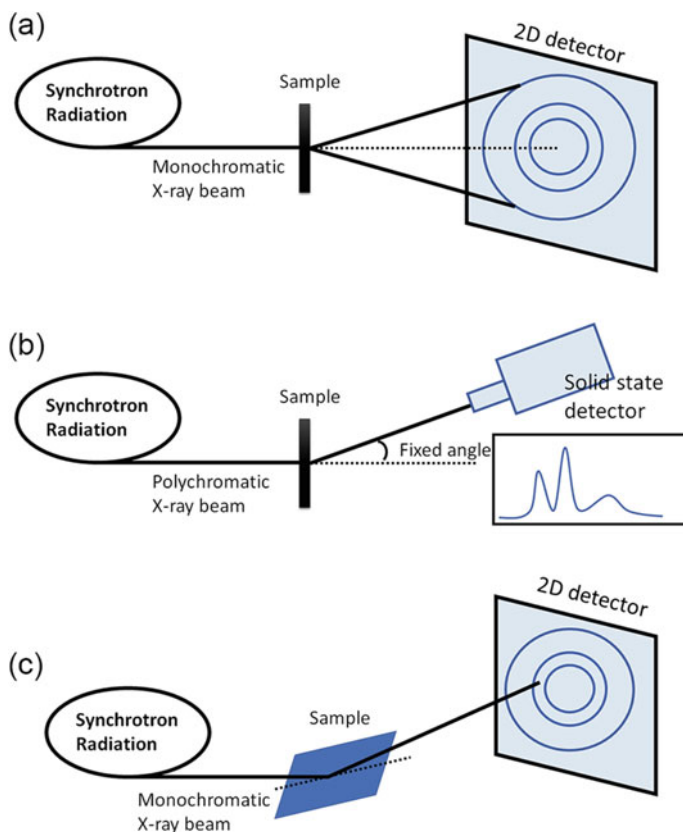


Fig. 6.9 Schematic illustration of the experimental layout in **a** ADXRD, **b** EDXRD, and **c** GIXRD

at a fixed angle. Using the high penetrating X-ray from the synchrotron source, the change of crystal structure of materials can be tracked from deep within the sample. It allows study of deep strain profiling and material phase changes under extreme conditions. The fast data acquisition rate using EDXRD mode (because there is no need to move the detector mechanically during data collection) is ideal for materials that are unstable under X-ray, and for capturing structural change during chemical reactions in situ. However, for thick samples or research that focus on the material surfaces (e.g. thin films), transmission detection mode is no longer applicable. In this case, a grazing incidence XRD (GIXRD) setup is adapted as shown in Fig. 6.9c, where the incident beam and detector sitting on the same side of the sample (similar to laboratory XRD).

Different from laboratory XRD, the synchrotron XRD data is often collected in 2D as a series of Debye-Scherrer rings (except EDXRD). Such image needs to be converted into the form as intensity vs diffraction angle. The most widely

used software for data conversion is FIT2D, which allows the 2D images to be integrated to 1D profile with user specified 2θ or radial direction. It also provides a variety of different output possibilities, such as several different 2θ scans, for different azimuth ranges; a 1D profile of intensity of a ring as a function of azimuth; or a polar transform of the data [67]. Once the 2D images were integrated as diffractions peaks, qualitative information in terms of crystalline phase, microstructures can be obtained by examining peak positions, peak shapes, intensities and so on.

In order to obtain quantitative structural parameters such as lattice constant, bond distance, and bond angles, the experimental data is fitted with a theoretical model, which can be fine-tuned to achieve the best match. One well-known method is called Rietveld refinement developed by Hugo Rietveld for use in the characterization of crystalline materials [68]. The Rietveld method uses a least squares approach to refine a theoretical line profile until it fits the measured profiles. The principle of the Rietveld method is to minimize a function M , defined in Eq. (6.6), which represents the difference between a calculated profile y^{calc} and the observed profile y^{obs} .

$$M = \sum_i W_i \left\{ y_i^{obs} - \frac{1}{c} y_i^{cals} \right\}^2 \quad (6.6)$$

where W_i is the statistical weight and c is an overall scale factor such that $y^{calc} = cy^{obs}$. The most used software for Rietveld refinement is the General Structure Analysis System (GSAS) [69]. Many programs are written to process Rietveld refinement, such as GSAS + EXPGUI [70], Fullprof and PowderCel, which can be used freely and are available on the internet. Other commercial programs such as MDI Jade and Bruker TOPAS are also available.

6.2.3.2 In Situ XRD: Probing The Real-Time Structure Change

As mentioned above, the deeper penetration depth of high energy synchrotron X-rays and the fast data acquisition is easy to achieve due to the high X-ray intensity, in situ XRD can be conducted to capture the crystal structure change in real time. In situ XRD has been employed to investigate structure of hybrid and inorganic LHPs. So far, research has been focusing on one of the two topics: (1) the real-time structure change of LHP during a chemical reaction, which is often related to the study of degradation mechanism of LHPs; [24, 71, 72] (2) the pressure-induced structural change emphasizing on new phase identification, and to modify the physical and chemical property of LHPs using high pressure [23, 73–89].

For instance, the degradation process of the $\text{CH}_3\text{NH}_3\text{PbI}_3$ in moist air was investigated by Yang and co-works utilizing ss GIXRD [71]. In their study, a hydrated intermediate phase containing isolated PbI_6^{4-} octahedral was identified as the first step of the degradation upon exposure of water vapor. Later, Zhao et al. designed an in situ cell to examine the stability of $\text{CH}_3\text{NH}_3\text{PbI}_3$ thin film in humid environment, shown in Fig. 6.10 [72]. They proposed a possible decomposition pathway

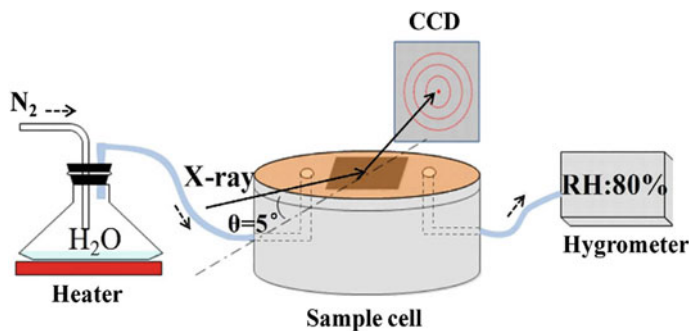


Fig. 6.10 Schematic diagram of the experimental setup for an in situ XRD measurement. Adapted from Ref. [72]



which agrees with Yang's result. This is a direct evidence that the monohydrated species is formed during the decomposition. A similar in situ setup was recently applied to investigate the humid effect on stability of inorganic lead bromide perovskite [24]. They observed an on-site phase transformation from Cs_4PbBr_6 to CsPbBr_3 and CsPb_2Br_5 and also revealed that such transformation process is probably controlled by both the solubility of CsBr and the coordination number of Pb(II) in water.

The other major application of in situ XRD is to monitor the high-pressure behavior of LHPs, focusing on pressure-induced phase transformation and pressure-induced modifications in electronic and optical properties of LHPs. A diamond anvil cell (DAC) is used to generate high pressure. This is done by applying a static mechanical force perpendicularly to the surface of the sample placed in a vessel. Among the many types of DACs, the widely employed high-pressure vessel is symmetric DAC as shown in Fig. 6.11. The sample was placed between a pair of diamonds anvils. The tips of the diamond anvils are only hundreds of microns in diameter. Therefore, a moderate force can generate several millions of atmospheres (e.g., 1 N can generate 8×10^6 Pa on a $400 \mu\text{m}$ culet.). The exact pressure values in the cell can be quantified using a pressure scale (e.g. ruby, Pt, Au). These materials have a known property that can be easily measured and has a direct correlation with applied pressure. For example, by exciting ruby with a green or blue laser, its fluorescence lines shift as a function of pressure [90]. Shown in Fig. 6.11c, during the measurement, a standard pressure scale (ruby ball) is loaded together with the sample of interest in the same DAC cell, and the real time structural change induced by pressure is then recorded by XRD.

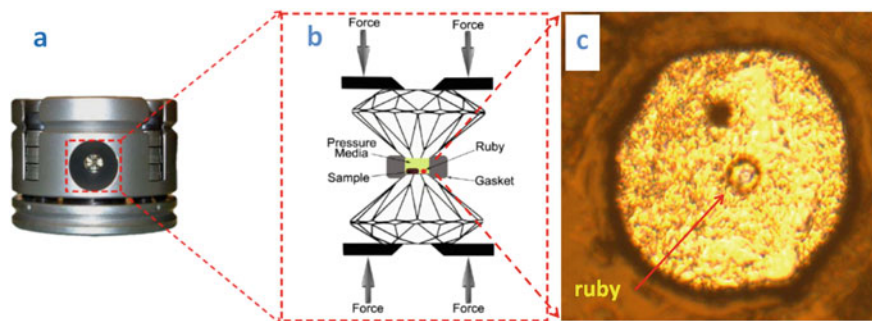


Fig. 6.11 **a** A photograph of a symmetric DAC, **b** schematic layout of a DAC (side view), **c** top view of the sample hole in the DAC with a ruby ball loaded

6.2.3.3 Pressure-Induced Phase Transformation

A great number of high-pressure study have been carried out on LHPs and it was found the LHPs exhibit interesting pressure-induced structural change that leads to modifications in electronic and optical properties.

The pressure induced phase transformation of LHPs were summarized in Table 6.2. Rich polymorph crystal structures produced in LHPs at high pressure were detected by various groups of researchers. However, the pressure-induced phase transformation sequences are inconsistent. For example, in Wang's study, MAPbCl_3 was found undergoing a phase transformation sequence from cubic ($Pm\bar{3}m$) to isostructured cubic phase ($Pm\bar{3}m$) at 0.8 GPa and then to an orthorhombic phase ($Pnma$) at 2.0 GPa [80]. However, another study suggests that MAPbCl_3 turns into a cubic ($Im\bar{3}$) phase at 0.75 GPa and then amorphizes directly at 2.0 GPa [81], while in Wang's study, amorphization was not observed until the pressure is above 5.6 GPa. The origin of these inconsistencies are not clear yet and more studies are needed.

Different from MAPbCl_3 , the phase transformation of MAPbBr_3 from cubic ($Pm\bar{3}m$) to cubic ($Im\bar{3}$) was observed in several studies, although such transformation occurs at slightly difference pressures, which is likely due to the difference in hydrostatic conditions used in different experiments [23, 81, 84, 88, 89]. The mechanism of such phase transformation is attributed to pressure-induced shrinkage and titling of the PbX_6^{2-} octahedra as well as the rotation of MA^+ cations. The isostructural phase transformation observed in MAPbCl_3 and MAPbI_3 more rely on rotation of the MA^+ cations [75, 79]. For MAPbI_3 , a pressure-induced metallization was also observed when the applied pressure is increased up to 60 GPa, and MAPbI_3 exhibits new transport properties [78].

Along with the structural change, perhaps the most interesting property of LHP is its band gap narrowing when pressure increases. This leads to elongated carrier lifetime and such narrowed band gap is retained after pressure is released [77]. It should also be addressed that the first pressure-induced phase transformation in all

Table 6.2 Summary of pressure induced phase transition in hybrid perovskites

Materials original phase		2nd Phase	3rd Phase	4th Phase	References	*Note
MAPbCl ₃	Cubic $Pm\bar{3}m$	Cubic ($Pm\bar{3}m$, 0.8GPa)*	Orthorhombic ($Pnma$, 2.0 GPa)	Amorphous (5.6 GPa)	[80]	Isostructural PT
		Cubic ($Im\bar{3}$, 0.75 GPa)	N/A	Amorphous (2.1 GPa)	[81]	
MAPbBr ₃	Cubic $Pm\bar{3}m$	Cubic ($Im\bar{3}$, 0.4 GPa)	Orthorhombic ($Pnma$, 1.8 GPa)	Amorphous (>2.0 GPa)	[23]	
		Cubic ($Im\bar{3}$, 1.0 GPa)	N/A	Amorphous (2.8 GPa)	[89]	
		Cubic ($Im\bar{3}$, 0.75 GPa)	N/A	Amorphous (2.7 GPa)	[81]	
		Cubic (s, 0.8 GPa)	N/A	Amorphous (4.7 GPa)	[88]	
		Cubic ($Im\bar{3}$, 0.9 GPa)	N/A	Amorphous (2.7 GPa)	[84]	
MAPbI ₃	Tetragonal $I4/mcm$	Cubic ($Im\bar{3}$, 0.3 GPa)	Orthorhombic ($Immm$, 2.7 GPa)	Amorphous (4.7 GPa)	[83]	
		Cubic ($Im\bar{3}$, 0.35 GPa)	N/A	Amorphous (2.5 GPa)	[81]	
		Cubic ($Im\bar{3}$, 0.35 GPa)	Cubic ($Im\bar{3}$, 2.5 GPa)*	N/A	[75]	Isostructural PT
	Orthorhombic $Fmmm$	Cubic ($Im\bar{3}$, 0.3 GPa)	N/A	Amorphous (3.4 GPa)	[84]	
FAPbBr ₃	Cubic $Pm\bar{3}m$	Cubic ($Im\bar{3}$, 0.53 GPa)	Orthorhombic ($Pnma$, 2.2 GPa)	Amorphous (4.0 GPa)	[79]	
FAPbI ₃	Cubic $Pm\bar{3}m$	Orthorhombic ($Imm2$, 0.34 GPa)	Orthorhombic ($Immm$, 2.7 GPa)	Amorphous (4.0 GPa)	[74]	
CsPbBr ₃	Orthogonal $Pbnm$	Orthogonal ($Pbnm$, 1.2 GPa)*	N/A	Amorphous (2.4 GPa)	[73]	Isostructural PT

Note PT stands for phase transformation. Phase transformations between structures with the same space group are transitions between two isostructural phases

LHP studied so far, occurs at a pressure below 1 GPa, especially for the cubic MAPbI₃ which can be obtained at a mild pressure of 0.35 GPa [75, 81, 83, 84]. This implies that modulation of LHP properties through applied pressure can be achieved without using DAC, and the phase transformation does not introduce additional chemical impurities, making this a practical and promising strategy of tuning the optical and electronic properties of LHPs.

6.3 Concluding Remarks

Synchrotron radiation technology has become an increasingly popular tool in materials characterization. It provides valuable information that cannot be obtained through laboratory techniques. This chapter summarizes three synchrotron X-ray techniques that have been used in studying LHP-based materials, which are X-ray absorption spectroscopy, X-ray excited optical luminescence, and X-ray diffraction. It should be noted that other synchrotron-based techniques, such as photoemission spectroscopy and X-ray scattering, are also employed in characterizing LHP-based devices, where LHPs are incorporated in the form of thin films. [26, 27, 91, 92]. These spectroscopic techniques allow detailed study on factors that influence charge transport in LHP films such as interface energetics and grain distribution. In addition, highly collimated X-rays from synchrotron source can also be produced with sub-micron spatial resolution. All the above-mentioned X-ray detection techniques can be conducted in the microscopy mode to obtain the local composition and structure of materials [93]. In summary, the fast advancement in synchrotron technology and analysis techniques provide an exciting future for characterization of LHPs. A deeper understanding on the fundamental properties of LHPs, the tunability of their structural and optical properties, and their stabilities in various environment will guide the development of LHP-based optoelectronic devices with outstanding performances.

References

1. I. Chung, B. Lee, J. He, R.P. Chang, M.G. Kanatzidis, *Nature* **485**, 486–489 (2012)
2. H.S. Jung, N.G. Park, *Small* **11**, 10–25 (2015)
3. Q. Zhang, Y. Yin, *ACS Central Sci.* **4**, 668–679 (2018)
4. L. Protesescu, S. Yakunin, M.I. Bodnarchuk, F. Krieg, R. Caputo, C.H. Hendon, R.X. Yang, A. Walsh, M.V. Kovalenko, *Nano Lett.* **15**, 3692–3696 (2015)
5. A. Kojima, K. Teshima, Y. Shirai, T. Miyasaka, *J. Am. Chem. Soc.* **131**, 6050–6051 (2009)
6. D. Shi, V. Adinolfi, R. Comin, M. Yuan, E. Alarousu, A. Buin, Y. Chen, S. Hoogland, A. Rothenberger, K. Katsiev, Y. Losovyj, X. Zhang, P.A. Dowben, O.F. Mohammed, E.H. Sargent, O.M. Bakr, *Science* **347**, 519–522 (2015)
7. M.A. Green, A. Ho-Baillie, H.J. Snaith, *Nat. Photonics* **8**, 506–514 (2014)
8. C. Bi, S. Wang, Q. Li, S.V. Kershaw, J. Tian, A.L. Rogach, *J. Phys. Chem. Lett.* **10**, 943–952 (2019)
9. J.S. Yao, J. Ge, B.N. Han, K.H. Wang, H.B. Yao, H.L. Yu, J.H. Li, B.S. Zhu, J.Z. Song, C. Chen, Q. Zhang, H.B. Zeng, Y. Luo, S.H. Yu, *J. Am. Chem. Soc.* **140**, 3626–3634 (2018)
10. W. Liu, Q. Lin, H. Li, K. Wu, I. Robel, J.M. Pietryga, V.I. Klimov, *J. Am. Chem. Soc.* **138**, 14954–14961 (2016)
11. P.J.S. Rana, T. Swetha, H. Mandal, A. Saeki, P.R. Bangal, S.P. Singh, *J. Phys. Chem. C* **123**, 17026–17034 (2019)
12. D. Bryant, N. Aristidou, S. Pont, I. Sanchez-Molina, T. Chotchunangatchaval, S. Wheeler, J.R. Durrant, S.A. Haque, *Energy Environ. Sci.* **9**, 1655–1660 (2016)
13. B. Conings, J. Drijkoningen, N. Gauquelin, A. Babayigit, J. D’Haen, L. D’Olieslaeger, A. Ethirajan, J. Verbeeck, J. Manca, E. Mosconi, F. De Angelis, H.G. Boyen, *Adv. Energy Mater.* **5**, 1500477 (2015)

14. B. Salhi, Y.S. Wudil, M.K. Hossain, A. Al-Ahmed, F.A. Al-Sulaiman, *Renew. Sustain. Energy Rev.* **90**, 210–222 (2018)
15. S. Huang, Z. Li, B. Wang, N. Zhu, C. Zhang, L. Kong, Q. Zhang, A. Shan, L. Li, *A.C.S. Appl. Mater. Interfaces* **9**, 7249–7258 (2017)
16. J. Pan, S.P. Sarmah, B. Murali, I. Dursun, W. Peng, M.R. Parida, J. Liu, L. Sinatra, N. Alyami, C. Zhao, E. Alarousu, T.K. Ng, B.S. Ooi, O.M. Bakr, O.F. Mohammed, *J. Phys. Chem. Lett.* **6**, 5027–5033 (2015)
17. Z. Shi, J. Guo, Y. Chen, Q. Li, Y. Pan, H. Zhang, Y. Xia, W. Huang, *Adv. Mater.* **29**, 1605005 (2017)
18. L. Liang, P. Gao, *Adv. Sci.* **5**, 1700331 (2018)
19. W. Xu, L. Liu, L. Yang, P. Shen, B. Sun, J.A. McLeod, *Nano Lett.* **16**, 4720–4725 (2016)
20. M.-C. Jung, Y.M. Lee, H.-K. Lee, J. Park, S.R. Raga, L.K. Ono, S. Wang, M.R. Leyden, B.D. Yu, S. Hong, Y. Qi, *Appl. Phys. Lett.* **108**, 073901 (2016)
21. J.A. McLeod, Z. Wu, B. Sun, L. Liu, *Nanoscale* **8**, 6361–6368 (2016)
22. J. Ma, Q. Yao, J.A. McLeod, L.Y. Chang, C.W. Pao, J. Chen, T.K. Sham, L. Liu, *Nanoscale* **11**, 6182–6191 (2019)
23. Y. Wang, X. Lu, W. Yang, T. Wen, L. Yang, X. Ren, L. Wang, Z. Lin, Y. Zhao, *J. Am. Chem. Soc.* **137**, 11144–11149 (2015)
24. M. Liu, J. Zhao, Z. Luo, Z. Sun, N. Pan, H. Ding, X. Wang, *Chem. Mater.* **30**, 5846–5852 (2018)
25. B. Philippe, B.-W. Park, R. Lindblad, J. Oscarsson, S. Ahmadi, E.M.J. Johansson, H. Rensmo, *Chem. Mater.* **27**, 1720–1731 (2015)
26. V.K. Ravi, P.K. Santra, N. Joshi, J. Chugh, S.K. Singh, H. Rensmo, P. Ghosh, A. Nag, *J. Phys. Chem. Lett.* **8**, 4988–4994 (2017)
27. W. Huang, F. Huang, E. Gann, Y.-B. Cheng, C. McNeill, *Adv. Funct. Mater.* **25**, 5529–5536 (2015)
28. C.Y. Chang, Y.C. Huang, C.S. Tsao, W.F. Su, *A.C.S. Appl. Mater. Interfaces* **8**, 26712–26721 (2016)
29. G. Bunker, *Introduction to XAFS: A Practical Guide to X-Ray Absorption Fine Structure Spectroscopy* (Cambridge University Press, New York, 2010)
30. P. Willmott, *Spectroscopic Techniques, An Introduction to Synchrotron Radiation: Techniques And Applications* (John Wiley & Sons Ltd, UK, 2019)
31. An online version of the booklet is available at: <https://xdb.lbl.gov/>
32. E.A. Stern, D.E. Sayers, F.W. Lytle, *Phys. Rev. B* **11**, 4836–4846 (1975)
33. J.J. Rehr, R.C. Albers, *Rev. Mod. Phys.* **72** (2000)
34. Z. Sun, Q. Liu, T. Yao, W. Yan, S. Wei, *Sci. Chin. Mater.* **58**, 313–341 (2015)
35. J.A. McLeod, Z. Wu, P. Shen, B. Sun, L. Liu, *J. Phys. Chem. Lett.* **5**, 2863–2867 (2014)
36. Y. Wang, Z. Xia, L. Liu, W. Xu, Z. Yuan, Y. Zhang, H. Sirringhaus, Y. Lifshitz, S.T. Lee, Q. Bao, B. Sun, *Adv. Mater.* **29**, 1606370 (2017)
37. P. Shen, K. Nie, X. Sun, L. Liu, J.A. McLeod, *Phys. Stat. Sol. RRL* **10**, 677–681 (2016)
38. L. Etgar, P. Gao, Z. Xue, Q. Peng, A.K. Chandiran, B. Liu, M.K. Nazeeruddin, M. Gratzel, *J. Am. Chem. Soc.* **134**, 17396–17399 (2012)
39. S.D. Stranks, G.E. Eperon, G. Grancini, C. Menelaou, M.J. Alcocer, T. Leijtens, L.M. Herz, A. Petrozza, H.J. Snaith, *Science* **342**, 341–344 (2013)
40. J.M. Frost, K.T. Butler, F. Brivio, C.H. Hendon, M. van Schilfgaarde, A. Walsh, *Nano Lett.* **14**, 2584–2590 (2014)
41. G. Niu, X. Guo, L. Wang, *J. Mater. Chem. A* **3**, 8970–8980 (2015)
42. Q. Wang, R. Wang, P. Shen, C. Li, Y. Li, L. Liu, S. Duhm, J. Tang, *Adv. Mater. Interfaces* (2015)
43. S.R. Raga, M.-C. Jung, M.V. Lee, M.R. Leyden, Y. Kato, Y. Qi, *Chem. Mater.* **27**, 1597–1603 (2015)
44. T.-W. Ng, C.-Y. Chan, M.-F. Lo, Z.Q. Guan, C.-S. Lee, *J. Mater. Chem. A* (2015)
45. R. Wang, C. Wu, Y. Hu, J. Li, P. Shen, Q. Wang, L. Liao, L. Liu, S. Duhm, *A.C.S. Appl. Mater. Interfaces* **9**, 7859–7865 (2017)

46. N.K. Kim, Y.H. Min, S. Noh, E. Cho, G. Jeong, M. Joo, S.W. Ahn, J.S. Lee, S. Kim, K. Ihm, H. Ahn, Y. Kang, H.S. Lee, D. Kim, *Sci. Rep.* **7**, 4645 (2017)
47. G. Grancini, A.R. Srimath Kandada, J.M. Frost, A.J. Barker, M. De Bastiani, M. Gandini, S. Marras, G. Lanzani, A. Walsh, A. Petrozza, *Nat. Photonics*, **9**, 695–701 (2015)
48. E.J. Juarez-Perez, Z. Hawash, S.R. Raga, L.K. Ono, Y. Qi, *Energy Environ. Sci.* **9**, 3406–3410 (2016)
49. G. Abdelmageed, L. Jewell, K. Hellier, L. Seymour, b. Luo, F. Bridges, J.Z. Zhang, S. Carter, *Appl. Phys. Lett.* **109**, 233905 (2016)
50. G. Abdelmageed, C. Mackeen, K. Hellier, L. Jewell, L. Seymour, M. Tingwald, F. Bridges, J.Z. Zhang, S. Carter, *Sol. Energy Mater. Sol. Cells* **174**, 566–571 (2018)
51. J. Kim, S.-H. Lee, J.H. Lee, K.-H. Hong, *J. Phys. Chem. Lett.* **5**, 1312–1317 (2014)
52. W.-J. Yin, T. Shi, Y. Yan, *Appl. Phys. Lett.* **104**, 063903 (2014)
53. C.-C. Chueh, C.-Y. Liao, F. Zuo, S.T. Williams, P.-W. Liang, A.K.Y. Jen, *J. Mater. Chem. A* **3**, 9058–9062 (2015)
54. Q. Chen, H. Zhou, Y. Fang, A.Z. Stieg, T.B. Song, H.H. Wang, X. Xu, Y. Liu, S. Lu, J. You, P. Sun, J. McKay, M.S. Goorsky, Y. Yang, *Nature Commun.* **6**, 7269 (2015)
55. S. Das Adhikari, S.K. Dutta, A. Dutta, A.K. Guria, N. Pradhan, *Angew. Chem.* **56**, 8746–8750 (2017)
56. A. Ishii, T. Miyasaka, *Adv. Sci.* **7**, 1903142 (2020)
57. H. Shao, X. Bai, H. Cui, G. Pan, P. Jing, S. Qu, J. Zhu, Y. Zhai, B. Dong, H. Song, *Nanoscale* **10**, 1023–1029 (2018)
58. Z.J. Yong, S.Q. Guo, J.P. Ma, J.Y. Zhang, Z.Y. Li, Y.M. Chen, B.B. Zhang, Y. Zhou, J. Shu, J.L. Gu, L.R. Zheng, O.M. Bakr, H.T. Sun, *J. Am. Chem. Soc.* **140**, 9942–9951 (2018)
59. G.H. Ahmed, J.K. El-Demellawi, J. Yin, J. Pan, D.B. Velusamy, M.N. Hedhili, E. Alarousu, O.M. Bakr, H.N. Alshareef, O.F. Mohammed, *ACS Energy Lett.* **3**, 2301–2307 (2018)
60. J.-P. Ma, Y.-M. Chen, L.-M. Zhang, S.-Q. Guo, J.-D. Liu, H. Li, B.-J. Ye, Z.-Y. Li, Y. Zhou, B.-B. Zhang, O.M. Bakr, J.-Y. Zhang, H.-T. Sun, *J. Mater. Chem. C* **7**, 3037–3048 (2019)
61. T.K. Sham, D.T. Jiang, I. Coulthard, J.W. Lorimer, X.H. Feng, K.H. Tan, S.P. Frigo, R.A. Rosenberg, D.C. Houghton, B. Bryskiewicz, *Nature*, **363**, 331–334 (1993)
62. L. Armelao, F. Heigl, A. Jurgensen, R.I.R. Blyth, T. Regier, X.T. Zhou, T.K. Sham, *J. Phys. Chem. C* **111**, 10194–10200 (2007)
63. Y. Hu, A. Mcaclennan, T.K. Sham, *J. Luminescence* **166**, 143–147 (2015)
64. L. Liu, T.K. Sham, in *Titanium Dioxide: Material for a Sustainable Environment*, ed. by D. Yang, *Luminescence from TiO₂ Nanotubes And Related Nanostructures Investigated using Synchrotron X-Ray Absorption Near-Edge Structure and X-ray Excited Optical Luminescence* (IntechOpen, 2017)
65. L. Liu, J. Li, T.-K. Sham, *Can. J. Chem.* **93**, 106–112 (2015)
66. A.K. Guria, S.K. Dutta, S.D. Adhikari, N. Pradhan, *ACS Energy Lett.* **2**, 1014–1021 (2017)
67. A.P. Hammersley, S.O. Svensson, M. Hanfland, A.N. Fitch, D. Hausermann, *High Pressure Research* **14**, 235–248 (1996)
68. L.B. McCusker, R.B. von Dreele, D.E. Cox, D. Louer, P. Scardi, *J. Appl. Cryst.* **32**, 36–50 (1999)
69. A.C. Larson, R.B. Von Dreele, Los Alamos National Laboratory Report, Los Alamos National Laboratory (2000)
70. B.H. Toby, *J. Appl. Cryst.* **34**, 210–213 (2001)
71. J. Yang, B.D. Siempelkamp, D. Liu, T.L. Kelly, *ACS Nano* **9**, 1955–1963 (2015)
72. J. Zhao, B. Cai, Z. Luo, Y. Dong, Y. Zhang, H. Xu, B. Hong, Y. Yang, L. Li, W. Zhang, C. Gao, *Sci. Rep.* **6**, 21976 (2016)
73. L. Zhang, Q. Zeng, K. Wang, *J. Phys. Chem. Lett.* **8**, 3752–3758 (2017)
74. P. Wang, J. Guan, D.T.K. Galeschuk, Y. Yao, C.F. He, S. Jiang, S. Zhang, Y. Liu, M. Jin, C. Jin, Y. Song, *J. Phys. Chem. Lett.* **8**, 2119–2125 (2017)
75. M. Szafranski, A. Katrusiak, *J. Phys. Chem. Lett.* **7**, 3458–3466 (2016)
76. P. Postorino, L. Malavasi, *J. Phys. Chem. Lett.* **8**, 2613–2622 (2017)

77. G. Liu, L. Kong, J. Gong, W. Yang, H.-K. Mao, Q. Hu, Z. Liu, R.D. Schaller, D. Zhang, T. Xu, *Adv. Funct. Mater.* **27**, 1604208 (2017)
78. A. Jaffe, Y. Lin, W.L. Mao, H.I. Karunadasa, *J. Am. Chem. Soc.* **139**, 4330–4333 (2017)
79. L. Wang, K. Wang, B. Zou, *J. Phys. Chem. Lett.* **7**, 2556–2562 (2016)
80. L. Wang, K. Wang, G. Xiao, Q. Zeng, B. Zou, *J. Phys. Chem. Lett.* **7**, 5273–5279 (2016)
81. M. Szafranski, A. Katrusiak, *J. Phys. Chem. Lett.* **8**, 2496–2506 (2017)
82. X. Lu, Y. Wang, C.C. Stoumpos, Q. Hu, X. Guo, H. Chen, L. Yang, J.S. Smith, W. Yang, Y. Zhao, H. Xu, M.G. Kanatzidis, Q. Jia, *Adv. Mater.* **28**, 8663–8668 (2016)
83. S. Jiang, Y. Fang, R. Li, H. Xiao, J. Crowley, C. Wang, T.J. White, W.A. Goddard 3rd., Z. Wang, T. Baikie, J. Fang, *Angew. Chem.* **55**, 6540–6544 (2016)
84. A. Jaffe, Y. Lin, C.M. Beavers, J. Voss, W.L. Mao, H.I. Karunadasa, *ACS Central Sci.* **2**, 201–209 (2016)
85. A. Jaffe, Y. Lin, W.L. Mao, H.I. Karunadasa, *J. Am. Chem. Soc.* **137**, 1673–1678 (2015)
86. Y. Lee, D. Mitzi, P. Barnes, T. Vogt, *Phys. Rev. B*, **68** (2003)
87. K. Gesi, *Ferroelectrics* **203**, 249–268 (1997)
88. K. Matsuishi, T. Ishihara, S. Onari, Y.H. Chang, C.H. Park, *Phys. Stat. Sol. (b)* **241**, 3328–3333 (2004)
89. I.P. Swainson, M.G. Tucker, D.J. Wilson, B. Winkler, V. Milman, *Chem. Mater.* **19**, 2401–2405 (2007)
90. A.D. Chijioke, W.J. Nellis, A. Soldatov, I.F. Silvera, *J. Appl. Phys.* **98**, 114905 (2005)
91. A.R. Milosavljevic, D.K. Bozanic, S. Sadhu, N. Vukmirovic, R. Dojcilovic, P. Sapkota, W. Huang, J. Bozek, C. Nicolas, L. Nahon, S. Ptasinska, *J. Phys. Chem. Lett.* **9**, 3604–3611 (2018)
92. L. Oesinghaus, J. Schlipf, N. Giesbrecht, L. Song, Y. Hu, T. Bein, P. Docampo, P. Müller-Buschbaum, *Adv. Mater. Interfaces* **3**, 1600403 (2016)
93. M. Kodur, R.E. Kumar, Y. Luo, D.N. Cakan, X. Li, M. Stuckelberger, D.P. Fenning, *Adv. Energy Mater.* 1903170 (2020)